

Topological Dirac Nodal Lines in fcc Calcium, Strontium, and Ytterbium

Motoaki Hirayama,^{1,2} Ryo Okugawa,¹ Takashi Miyake,³ and Shuichi Murakami^{*1,2}

¹Department of Physics, Tokyo Institute of Technology, Ookayama, Meguro-ku, Tokyo 152-8551, Japan

²TIES, Tokyo Institute of Technology, Ookayama, Meguro-ku, Tokyo 152-8551, Japan

³Research Center for Computational Design of Advanced Functional Materials, AIST, Tsukuba 305-8568, Japan
(Dated: September 9, 2016)

In nodal-line semimetals, which are among the classes of topological semimetals, the gap closes along loops in \mathbf{k} space, which are not at high-symmetry points. Typical mechanisms for emergence of nodal lines are either from mirror symmetry or from π Berry phase, and the latter is achieved only in systems without spin-orbit interaction, with inversion and time-reversal symmetries. So far all the proposals of materials with nodal lines stem from mirror symmetry. Here we show by *ab initio* calculations that fcc Ca, Sr, and Yb have topological nodal lines near the Fermi level when the spin-orbit interaction is neglected. These nodal lines do not originate from mirror symmetry, and are topologically characterized by π Berry phase. Therefore, the Zak phase along a reciprocal lattice vector in \mathbf{k} space becomes either π or 0 depending on the momentum, and the π Zak phase is related to bulk charge polarization, appearing as surface polarization. It is eventually screened by the carriers, leaving behind large dipoles at the surface. In Ca at high pressure, only the nodal lines lie at the Fermi level, and it is a nodal-line semimetal. In the materials having the nodal lines, both the large polarization and the emergent “drumhead” surface states enhance the Rashba splitting when adatoms with large spin-orbit interactions are present, as we show in Bi/Sr(111) and in the well-known giant Rashba system Bi/Ag(111).

Introduction—Recent discoveries of topological semimetals have taught us that the \mathbf{k} -space topological structure of the electronic bands plays a vital role in a number of materials. This material class of topological semimetals includes Weyl semimetals[1, 2], Dirac semimetals[3, 4], and nodal-line semimetals (NLS’s) [5, 7–15, S4]. In topological semimetals, the conduction and valence bands touch each other at some generic points (Dirac and Weyl semimetals) or along curves (NLS) in \mathbf{k} -space, and such degeneracies do not originate from high-dimensional irreducible representations in such \mathbf{k} point but from interplay between \mathbf{k} -space topology and symmetry. The Dirac semimetals are realized in Na_3Bi [16, 17] and Cd_3As_2 [18, 19]. The Weyl semimetals are proposed in pyrochlore iridates[2], HgCr_2Se_4 [20], Te under pressure[21], $\text{LaBi}_{1-x}\text{Sb}_x\text{Te}_3$, $\text{LuBi}_{1-x}\text{Sb}_x\text{Te}_3$ [22], transition-metal dichalcogenides[23, 24], and SrSi_2 [25] as real materials. Recently, TaAs class materials, after the theoretical prediction[26, 27], are experimentally observed as Weyl semimetals[28–32].

Here we focus on NLS. Two typical origins of the nodal lines are classified into two, i.e. (A) mirror symmetry and (B) π Berry phase, as explained in Methods section. To our knowledge, the proposals for the NLS’s so far are restricted to the case (A), mirror symmetry. Among the Dirac NLS, having the Kramers degeneracy, are carbon allotropes[7, 8], Cu_3PdN [9, 10], Ca_3P_2 [11, 12], LaN [13], CaAgX ($\text{X}=\text{P}, \text{As}$)[14], compressed black phosphorus[15] while the Weyl NLS contains HgCr_2Se_4 [20] and TiTaSe_2 [33]. In some of the proposed materials, the mechanism (B) coexists, and even if the mirror symmetry is broken externally, the loop will survive. So far no purely topological NLS, from the mechanism (B), has been proposed,

In this article, we propose by *ab initio* calculation that the alkaline earth metals Ca, Sr, Yb have topological nodal lines when the spin-orbit interaction (SOI) is neglected. In reality

the SOI is nonzero, especially for Yb, giving rise to a small gap along the otherwise gapless nodal lines. In fact the existence of nodal lines has been noticed in refs. 34 and 35, and it is used for explanation of resistivity data. Nevertheless, its topological origin and its relationship with surface states are left unexplored. Here we show their physical origin.

We also calculate the Zak phase along some reciprocal lattice vector and show that the Zak phase is either π or 0 depending on the momentum regions divided by the nodal lines. As the Zak phase is related with polarization, the region with π Zak phase gives rise to polarization charge at the surface normal to the reciprocal lattice vector. We show that the $0/\pi$ Zak phase is not related with the absence/presence of surface states, as is contrary to common belief. On the other hand the π Zak phase implies a polarization from the bulk states. It results in emergence of surface polarization charge. As is different from insulators, this surface polarization charge is screened by carriers and it will leave behind surface dipoles.

Finally we show that this large dipole due to the nodal lines induces a large Rashba splitting (Rashba energy: $E_R \sim 100$ meV) in the Bi/Sr(111) surface. In addition, the Bi/Ag(111) surface known for its large Rashba splitting ($E_R \sim 200$ meV) [36] is also attributed to hybridization between the Bi states with emergent surface states from the nodal lines in Ag. Thus the nodal lines are favorable for realizing large Rashba splitting, which is potentially important for spintronics applications.

Band structure of Ca, Sr and Yb—Ca, Sr, and Yb are non-magnetic metals, having face-centered cubic (fcc) lattice with a lattice parameter a (Fig. 1a). The space group of fcc is $\text{Fm}\bar{3}\text{m}$ (No. 225). At higher pressure, interesting phase transitions have been observed for these metals. In Yb, the metal-insulator transition takes place at 1.2 GPa [37]. Ca and Sr also show semimetallic behavior under pressure [38, 39]. First structural transition from fcc to body-centered cubic (bcc)

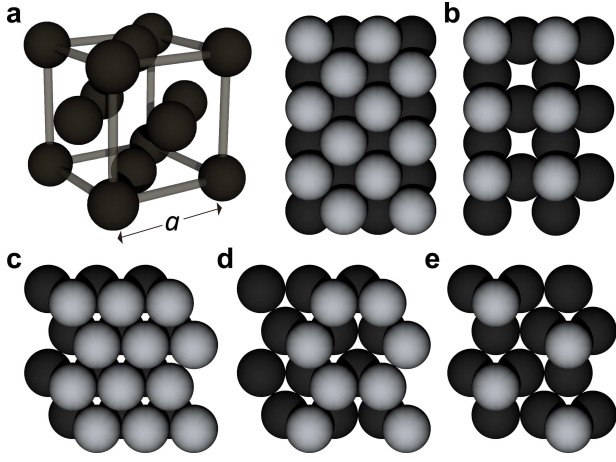


FIG. 1. **Bulk and surface structure.** **a**, Crystal structure of fcc Ca, Sr, and Yb, and that of the (001) surface (black circle) with surface atoms (gray circle). **b** shows the same surface orientation but with (1/2) atoms per unit cell on the surface. **c**, Crystal structure of the (111) surface (black circle) with surface atoms (gray circle). **d** and **e** show the same surface orientation but with (2/3) and (1/3) atoms per unit cell on the surface, respectively.

takes place 19-20 GPa in Ca [40]. The high temperature superconductivity is observed at 29 K in Ca at 216 GPa after several structural transitions [41].

We calculate their electronic structures within *ab initio* calculations explained in Methods section. Figure 2a shows the electronic structure of Ca in the local density approximation (LDA). The Brillouin zone is shown as a truncated octahedron in Fig. 2b. In a Ca atom, a gap exists between fully occupied 4s and unoccupied 3d and 4p orbitals. When the atoms form a crystal, these orbitals form bands with the narrow- or pseudo-gap near the Fermi level. The top of the valence band, which is relatively flat near the L points, originates from the *p*-orbital oriented along the [111]-axis having a strong σ -bonding, while most of other valence bands originate from the *s*- and *d*-orbitals. Around the L points, the relatively flat valence band crosses the dispersive conduction bands. It gives four nodal lines around the L points within about ± 0.01 eV near the Fermi level, shown in Fig. 2b. (There seem to be eight nodal lines, but the nodal lines in the same colors are identical.) The four nodal lines are mutually related by the C_4 symmetry, and are slightly away from the faces of the first Brillouin zone, except for the points along the L-W lines (Q_1 in Fig. 2c) due to C_2 symmetry. The nodal lines do not lie on mirror planes, and therefore they do not come from mirror symmetry, but from topology; indeed, we numerically confirmed as the π Zak phase around the nodal lines.

We also calculate the \mathbb{Z}_2 indices [9] from the parity eigenvalues of the valence bands at the time-reversal invariant momenta (TRIM), and all the \mathbb{Z}_2 indices are even (trivial) for Ca, Sr, and Yb. The existence of the nodal lines is consistent with the trivial \mathbb{Z}_2 indices, since the number of the nodal lines between the TRIM is even. In that sense, these met-

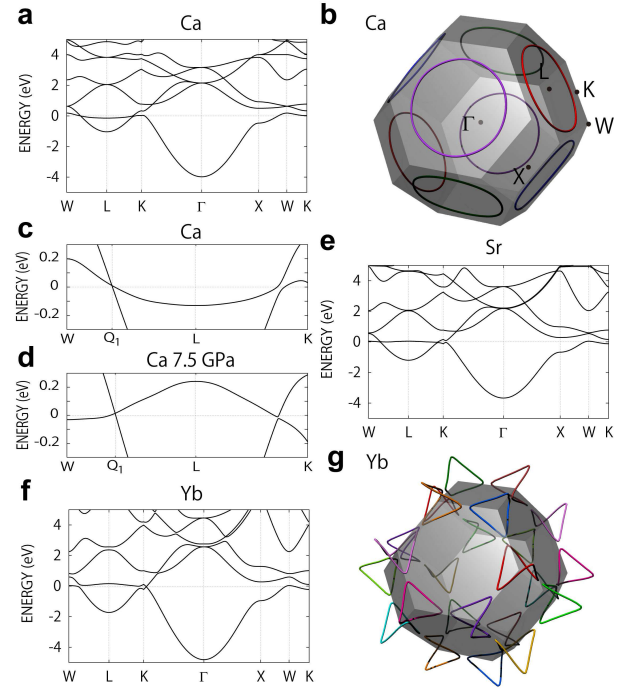


FIG. 2. **Electronic band structure and nodal line.** **a**, Electronic band structure of Ca in the LDA. **b**, Nodal lines and the Brillouin zone of Ca, where the identical nodal lines (modulo reciprocal vector) are shown in the same color. **c/d** is the magnified electronic band structure of Ca at ambient pressure/at 7.5 GPa in the LDA. **e** and **f** are electronic band structures of Sr and Yb in the LDA+SO, respectively. **g** is the nodal lines of Yb in the LDA. The energy is measured from the Fermi level.

als are “weak” NLS, and the existence of nodal lines do not come from bulk \mathbb{Z}_2 indices. Another \mathbb{Z}_2 index is defined in Ref. [S4]. It is defined for each nodal line, and if it is non-trivial it prohibits the nodal line from disappearing by itself. In the present case of Ca, this \mathbb{Z}_2 index is trivial, as shown in detail in the Supplemental Material.

At ambient pressure, Ca is not a NLS, because the two bands forming the nodal lines are both dispersing downward around the L points (Fig. 2c). Meanwhile, Ca becomes a NLS under pressure, as shown in the band structure at 7.5 GPa in Fig. 2d; the similar conclusion was reached in refs 34 and 35 without giving the origin of the nodal lines. Here the pressure increases the energy of the *p*-orbital against that of the *s*- and *d*-orbitals.

The electronic structure of Sr in the LDA+SO is shown in Fig. 2e. The SOI is not strong in the whole k -space. The band at the L points near the Fermi level is relatively flat compared to that in Ca because the energy difference between the 5*s*-, 4*d*- and 5*p*-orbitals is larger than that between the 4*s*-, 3*d*- and 4*p*-orbitals. If the SOI is neglected, four nodal lines around the L points exist, as is the case with Ca. The nodal line is fully gapped with the SOI; for example, the degeneracy on the L-W line splits about 0.04 eV by the SOI.

Figure 2f shows the electronic structure of Yb in the

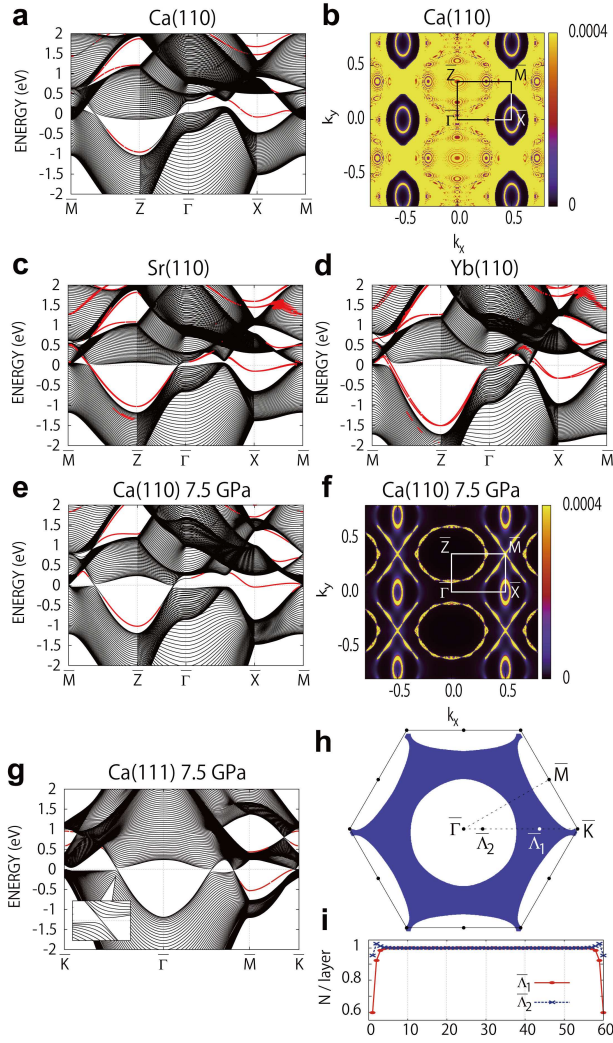


FIG. 3. **Topological surface state and polarization.** **a**, Electronic band structure of Ca for the (110) surface in the LDA. The symmetry points are $\bar{\Gamma} = (0, 0, 0)$, $\bar{X} = \pi/a(\sqrt{2}, 0, 0)$, $\bar{Z} = \pi/a(0, 0, 1)$, and $\bar{M} = \pi/a(\sqrt{2}, 0, 1)$. **b**, The intensity color plot of the charge distribution in k space at the Fermi level within one atomic layer near the surface (unit for the k vector is $2\sqrt{2}\pi/a$). **c** and **d** are the electronic band structure of Sr and Yb for the (110) surface in the LDA+SO, respectively. **e/f** is the result of Ca at 7.5 GPa corresponding to **a/b**. **g**, Electronic band structure of Ca for the (111) surface in the LDA, with the states close to the nodal line is magnified in the inset. **h**, Dependence of the Zak phase on the surface momentum k_{\parallel} . The shaded region represents k_{\parallel} with π Zak phase, while other regions represent that with 0 Zak phase. **i**, Charge profile in real space over the thickness of the slab, for two values of the surface momentum $k_{\parallel} = \bar{\Lambda}_1, \bar{\Lambda}_2$. The vertical axis represents the charge density per surface unit cell within each atomic layer, measured in the unit of the electronic charge $-e$. In **a,c,d,e,g**, the wave functions monotonically decreasing toward the bulk region are shown in red. The energy is measured from the Fermi level.

LDA+SO. The energy splitting on the L-W line reaches about 0.2 eV. Unlike Ca and Sr, The nodal lines without the SOI in Yb are qualitatively different from those in Ca and Sr; hybridization between four nodal lines around the X points causes a Lifshitz transition, i.e. a recombination of the nodal lines, and small twelve nodal lines appear around the W points (Fig. 2g). Similar recombination of nodal lines is seen when the lattice constant of Ca crystal is enlarged in numerical calculation, which gradually reduces the crystal to the atomic limit. First the nodal lines are formed around the W points after a recombination. Then they shrink toward the W points and disappear. Thus, as compared with Ca and Sr, Yb is closer to band inversion between the atomic limit and the crystal.

Zak phase and surface states— We now show surface states of Ca, Sr, and Yb. Figure 3a shows the electronic structure of the Ca(110) surface, and its charge distribution at the Fermi level is shown in Fig. 3b. Similar surface states are found also in the Sr(110) and Yb(110) surfaces (Fig. 3c,d). Surface states connecting between the gapless points exist near the Fermi level around the \bar{X} point, isolated from the bulk states. In particular, in Sr and Yb, while the SOI opens a small gap at the nodal lines, the surface states persist as a result of nodal lines by continuity. In this (110) surface, out of the four nodal lines, two overlap each other, resulting in a projected nodal line around the \bar{Z} point. The other two nodal lines become almost segments crossing each other at the \bar{M} point. Figure 3e is the electronic structure of the Ca(110) surface at 7.5 GPa. It is in the NLS phase, and the states at the Fermi level (Fig. 3f) consist almost only of the surface states.

We calculate the Zak phase (the Berry phase), which is an integral of Berry connection of the bulk wavefunction along a fixed direction along a certain reciprocal vector \mathbf{G} . For the calculation, we decompose the wavevector \mathbf{k} into the components along $\mathbf{n} \equiv \mathbf{G}/|\mathbf{G}|$ and perpendicular to \mathbf{n} : $\mathbf{k} = k_{\perp}\mathbf{n} + \mathbf{k}_{\parallel}$, $\mathbf{k}_{\parallel} \perp \mathbf{n}$. The integral with respect to k_{\perp} is performed with fixed \mathbf{k}_{\parallel} . As discussed in Ref. [S3], this quantity is related with a polarization at surface momentum \mathbf{k}_{\parallel} for a surface perpendicular to \mathbf{n} (see Methods section for details). The Zak phase is defined modulo 2π due to a gauge degree of freedom. We focus on the cases without the SOI and neglect the spin degeneracy. The formula of the Zak phase, applied to one-dimensional insulating systems, is the polarization times $2\pi/e$ [S3]. In three-dimensional systems, one can also relate it with polarization. If one regards the three-dimensional system at each \mathbf{k}_{\parallel} as a one-dimensional system, the Zak phase $\theta(\mathbf{k}_{\parallel})$ is equal to $\frac{2\pi}{e}\sigma(\mathbf{k}_{\parallel})$ modulo 2π , where $\sigma(\mathbf{k}_{\parallel})$ is a charge at the surface for the one-dimensional system at given \mathbf{k}_{\parallel} . For an insulator, a surface polarization charge density σ_{total} at the given surface is given by $\sigma_{\text{total}} = \int \frac{d^2k_{\parallel}}{(2\pi)^2} \sigma(\mathbf{k}_{\parallel})$ [S3]. Because the Berry phase around the nodal line is π , the Zak phase jumps by π as \mathbf{k}_{\parallel} is changed across the nodal line. It is confirmed in our case. The resulting Zak phase is 0 in the whole \mathbf{k}_{\parallel} -space for the (110) surface, because the two nodal lines out of the four overlap with each other while the other two become almost segments. In the (001) surface, the Zak phase

is also 0 everywhere, because four nodal lines overlap each other in two pairs, and the Zak phase is doubled. Meanwhile, for the (111) surface (Fig. 3g), the Zak phase is π outside of the nodal line, as shown as the shaded region in Fig. 3h. and within this k_{\parallel} region with the π Zak phase, $\sigma(k_{\parallel})$ takes a value $\sigma(k_{\parallel}) \equiv e/2 \pmod{e}$ [S3], inevitably leading to a surface polarization charge. When the surface termination is fixed, the value of $\sigma(k_{\parallel})$ is determined without the indeterminacy modulo e .

For example, for $\bar{\Lambda}_1$ and $\bar{\Lambda}_2$ points in Fig. 3h, the Zak phases are π and 0, respectively, and the polarizations $\sigma(k_{\parallel})$ are $e/2$ and 0 ($\text{mod } e$). Since surface states exist neither at $\bar{\Lambda}_1$ nor at $\bar{\Lambda}_2$, this difference in polarization should be attributed to charge distribution of bulk valence bands, as demonstrated in Fig. 3i. At $\bar{\Lambda}_2$ the charge distribution is almost constant even near the surface, whereas at $\bar{\Lambda}_1$ it decreases by $\sim (-e)/2$ near each surface. It is consistent with the polarization $e/2 \text{ mod } e$. Since the two surfaces of the slab are equivalent due to inversion symmetry, the total charge at $\bar{\Lambda}_1$ is less than that at $\bar{\Lambda}_2$ by one electron (i.e. charge $(-e)$). It is attributed to one state, which traverses across the nodal line from the valence band to the conduction band along the $\bar{K} \rightarrow \bar{\Gamma}$ direction in the inset of Fig. 3g. (We note that this state is not a surface state, since it disappears in the limit of infinite system size. The small gap between \bar{K} and $\bar{\Gamma}$ is a minigap by finite-size effect and this gap goes to zero in the infinite system size.) Therefore, to summarize, $e/2$ polarization (π Zak phase) should be attributed to bulk states. It holds true even when it is not quantized; nonzero Zak phase θ implies that the BULK states have excess polarization charge at the surface.

Thus $\sigma(k_{\parallel})$ takes the value $\sigma(k_{\parallel}) = \frac{e}{2}$ in the shaded region in Fig. 3h, whose area is 0.485 of the total area of the Brillouin zone. Therefore, the surface polarization charge density $\sigma = 0.485 \cdot \frac{e}{2A_{\text{surface}}} \sim \frac{0.243e}{A_{\text{surface}}}$ where A_{surface} is the area of the surface unit cell. We note that it is a polarization charge if we consider the system as a collection of one-dimensional systems with each k_{\parallel} . In reality, because of the existence of carriers, the excess surface charge will be screened by the free carriers, as discussed later in this paper.

It is commonly believed that when $\theta(k_{\parallel})$ equals to π at some k_{\parallel} , the “drumhead” surface states appear at k_{\parallel} , and it is indeed the case if the system has chiral symmetry, by using the theorem in ref. 44. (Here surface states are defined as states having a finite penetration depth in the limit of an infinite system size.) Nevertheless, it is not always true in general systems. From a comparison between the (111) surface states (Fig. 3g) and the Zak phase (Fig. 3h), there is no direct relationship between the absence/presence of the surface states and the $0/\pi$ Zak phase. It is in fact natural from the following discussion. Suppose there is a surface state within the gap at k_{\parallel} near the nodal line. Then, if it is occupied it contributes by $(-e)$ to the surface polarization charge, and if unoccupied it does not contribute. Thus, the presence/absence or occupancy of surface states affects the surface polarization charge by an integer multiple of e . Thus it cannot account for $e/2$ polarization from the π Zak phase. Thus the π Zak phase (due to the nodal line) does not

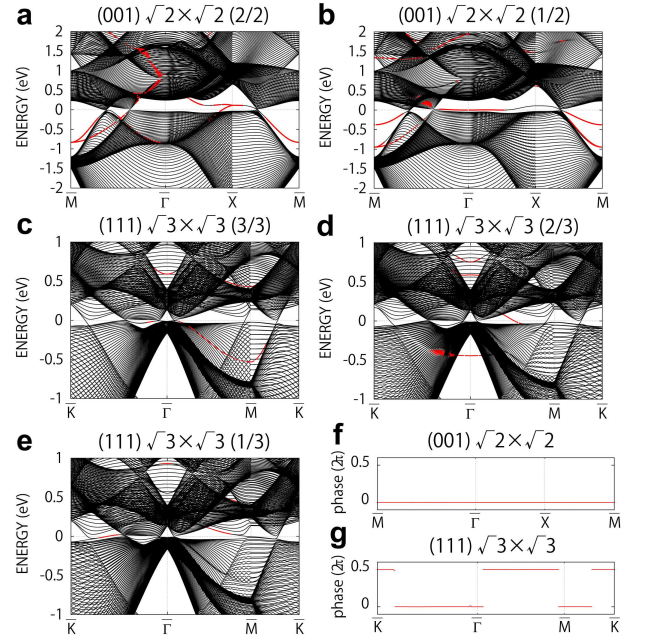


FIG. 4. Topological surface state on long-range superstructure. **a,b,c,d,e**, Electronic band structure of Ca at 7.5 GPa with long-range $\sqrt{2} \times \sqrt{2}/\sqrt{3} \times \sqrt{3}$ structure on the (001)/(111) surface in the LDA. The surface of **a,c** is flat, and that of **b,d/e** has (1/2)/(1/3)/(2/3) atoms per unit cell (**b, d** and **e** correspond to Fig. 1c, e, and f, respectively). The symmetry points in **a,b** are $\bar{\Gamma} = 2\pi/a(0, 0, 0)$, $\bar{X} = \pi/a(1, 0, 0)$, and $\bar{M} = \pi/a(1, 1, 0)$, and those in **c,d,e** are $\bar{\Gamma} = 2\sqrt{2}\pi/\sqrt{3}a(0, 0, 0)$, $\bar{M} = \sqrt{2}\pi/\sqrt{3}a(0, 1, 0)$, and $\bar{K} = \sqrt{2}\pi/\sqrt{3}a(\sqrt{3}, 1, 0)$. Wave functions decreasing monotonically toward the bulk region are shown in red. The energy is measured from the Fermi level. **f** is the Zak phase from the occupied bands corresponding to both **a** and **b**, giving the same results. Similarly, **g** is the Zak phase from the occupied bands corresponding to **c,d,e**, giving the same results.

imply existence of surface states, as has been noted also in Ref. S4, and presence/absence of surface states depends on details of the surface considered.

Only in systems with chiral symmetry, it is shown that the π Zak phase means presence of boundary states (at zero energy) [44]. It is consistent with our conclusion above. When the Zak phase for the bulk occupied bands at certain k_{\parallel} is π , the polarization of the occupied bands is $\sigma_{\text{occ.}} \equiv e/2 \pmod{e}$. By the chiral symmetry, the bulk unoccupied bands also have the same polarization $\sigma_{\text{unocc.}} = \sigma_{\text{occ.}}$. Therefore, the total polarization for all the bulk bands is $\sigma_{\text{unocc.}} + \sigma_{\text{occ.}} = 2\sigma_{\text{occ.}} \equiv e \pmod{2e}$. Thus there should be an odd number of surface states which accommodate excess electrons at a surface, and there should be a zero-energy surface state by chiral symmetry. Thus, the chiral symmetry is essential in relating the π Zak phase with the presence of surface states.

Next we consider the surfaces with some atoms depleted periodically, so that the surface forms superstructure. For the (001) surface, we consider two patterns for the $\sqrt{2} \times \sqrt{2}$ superstructure, shown in Fig. 1b,c: **b** represents the perfect surface while in **c** 1/2 of the surface atoms per unit cell are

present. For the (111) surface, we consider three patterns for the $\sqrt{3} \times \sqrt{3}$ superstructure, shown in Fig. 1d,e,f: d represents the perfect surface, and in e (f) $2/3$ ($1/3$) of the surface atoms per unit cell are present. The band structures are shown in Fig. 4a-e. We also found that for the (001) surface, two patterns for the $\sqrt{2} \times \sqrt{2}$, a and b, give the same Zak phase (see Fig. 4f). Similarly, for the (111) surface, three patterns for the $\sqrt{3} \times \sqrt{3}$ superstructure, c,d and e, give the same Zak phase (see Fig. 4g). While the Zak phase generally depends on the surface termination through the unit cell choice [S1], in the present cases, it is unchanged when the surface termination is changed for the fixed surface orientation, as shown in Supplemental materials. This result is natural because the bulk unit cell has a single atom, implying that the bulk polarization is uniquely determined.

Nodal lines and Rashba splitting— So far we have shown that the nodal lines affect the surface in two ways. One is through the bulk polarization. Across the nodal lines the Zak phase changes by π and there appear regions with π Zak phase ($e/2 \pmod{e}$ polarization) encircled by the nodal lines, giving rise to $\pm e/2$ surface polarization charge. The other is through the surface states. In some (but not all) cases the surface state emerges from the nodal lines. These two induce an appreciable amount of dipole at the surface, and are expected to enhance the surface Rashba splitting, as we show below.

We note that this property is special to materials with nodal lines. As a comparison, let us first consider an insulator with inversion and time-reversal symmetries. Then, the Zak phase satisfies $\theta(\mathbf{k}_{\parallel}) = N\pi$ (N : integer) (see Supplemental Materials). Because $\theta(\mathbf{k}_{\parallel})$ is continuous for all \mathbf{k}_{\parallel} , this integer N is common for all \mathbf{k}_{\parallel} . So far no insulator with $N \neq 0$ is known to our knowledge. It is possibly because of instability due to huge polarization; the Zak phase for even N is equivalent to $N = 0$. Hence nonzero even N is not protected, and is easily reduced to $N = 0$. Meanwhile, odd N means that the surface is covered by dangling bonds, which is expected to be quite unstable.

Meanwhile, in materials with nodal lines, the Zak phase jumps by π at the nodal lines, and therefore there are always two types of regions with $\theta(\mathbf{k}_{\parallel}) \equiv 0 \pmod{2\pi}$ and that with $\theta(\mathbf{k}_{\parallel}) \equiv \pi \pmod{2\pi}$. The latter region inevitably leads to an appreciable polarization, as is exemplified in Ca surface. In nodal-line semimetals, the bulk charges will eventually screen the polarization, but there occurs a large deformation of the lattice structure and electronic relaxation (i.e. screening). In the present case the surface polarizations are screened by carriers, leaving behind a dipole at the surface. As roughly estimated in Supplemental Material for calcium, the dipole density per surface unit cell is $\sim 5 \times 10^{-21} \text{C} \cdot \text{nm}$, a potential dip is $\sim -0.8 \text{eV}$ at the surface, and the electric field at the surface is $\sim 6.4 \text{V/nm}$.

Figure 5a shows the ratio of the interlayer distance at the surface to that of bulk for the several surfaces of fcc Ca and Sr and the (001) surface of hexagonal close-packed (hcp) Be and Mg. The surfaces of Ca and Sr, having nodal lines, are compressed near the surface by about 4 % (equivalent to that in

the bulk of Ca at $\sim 2 \text{GPa}$). This large compression in Ca and Sr might be associated with the polarization induced by the nodal lines, as we discuss in the following. From the above argument the effect of large charge imbalance at the surface is prominent only when the nodal lines are almost at the Fermi energy and no other Fermi surfaces exist. As shown in the Supplemental Material, the carriers in the semimetal screen the surface charge with a screening length of the order of nm. Thus the screening in this case is poor because the nodal-line semimetal has a small number of carriers, leaving behind an appreciable dipole moment at the surface after the screening. On the other hand, if there are carriers other than those forming the nodal-line, the screening effect is much more prominent, and dipoles will be small at the surface. In Be and Mg, there are nodal lines [45, 46] away from the Fermi level (at 0.0–1.1 eV in Be and at 0.6–1.1 eV in Mg, respectively), and the density of states at the Fermi energy is large, coming from the large Fermi surface, and therefore the compression of the lattice is small. Note that in addition to the (111) surface of Ca, the (001) and (110) surfaces also show large deformation, and they are attributed to large polarization, where some \mathbf{k} points with $0 \equiv 2\pi \pmod{2\pi}$ Zak phase are shown to have $-e$ polarization in our calculation (not shown). Thus the large compression is robust and almost independent of the surface termination. Furthermore, the electronic relaxation alters the surface state dispersions (Fig. 5b) as compared to the case with no relaxation (Fig. 3a), and energies of some surface states are lowered by about $\sim 1 \text{eV}$, which is attributed to the potential dip at the surface due to surface charge, estimated as $\sim -0.8 \text{eV}$. When the instability originating from the topological polarization is eliminated by covering the surface with alkali metal with small electronegativity, the surface states, shown in Fig. 5c, turn out to be almost the same as the original surface without relaxation (Fig. 3a).

We expect that such huge polarization by the nodal lines would enhance SOI spin-splitting at the surface. In Fig. 5d, we show the Rashba splitting in a monolayer Bi on the Sr(111) surface. The Rashba splitting of the surface Bi 6p bands near the Fermi level is $E_R \sim 100 \text{meV}$. Since the Sr(111) surface (not shown) does not have a surface state around $\bar{\Gamma}$ near the Fermi level (as is the case with Fig. 3g), we attribute this large splitting to the strong electric field from the nodal lines in addition to the difference in the electronegativity. The nodal lines brings about a potential dip at the surface, and it gives rise to additional strong electric field within the Bi layer, roughly of the order of $1 \text{V}/5\text{\AA} \sim 2 \text{V/nm}$. Such a strong additional electric field is expected to enhance the Rashba splitting. Nonetheless, it is difficult to evaluate the contribution of this additional electric field to the Rashba splitting, because the magnitude of the Rashba splitting is determined by the electric field very close to surface nuclei, and by the asymmetry of the wavefunctions of the surface atoms [47]. For comparison we give some examples; the Rashba parameter increases by 0.005 and 0.011 nm-eV under an external electric field $E = 4.0 \text{V/nm}$ in the Au(111) [48] and in the KTaO₃(001) surface [49], respectively. In the Bi/Sr(111) sur-

face, the Rashba parameter for the Bi $6p_z$ band is 0.071 nm-eV, a part of which would originate from the topological polarization.

As a comparison, we discuss the Bi/Ag(111) surface which is known to have a large Rashba splitting [36]. We can attribute this also to nodal lines in Ag, but by different mechanism from that in Bi/Sr(111). The conduction band structure of fcc Ag in Fig 5e closely resembles that of Ca, Sr, and Yb, and Ag also has topological Dirac nodal lines around 5 eV (Fig. 5f). The Dirac nodal lines give rise to surface states for the (111) surface, which are visible around $\bar{\Gamma}$ near the Fermi energy, shown in Fig. 5g. The well-known giant Rashba splitting is realized when $1/3$ of the surface Ag atoms are substituted by Bi atoms, forming the $\sqrt{3} \times \sqrt{3}$ structure [36]. To see its origin, in Fig. 5h we show the band structure for the $\sqrt{3} \times \sqrt{3}$ Ag(111) surface with $1/3$ of the surface Ag atoms are depleted (Fig. 1d); surface states also exist around 0.6 eV, which is higher than those in Fig. 5g because some of the bonds are depleted. The Bi/Ag(111) surface is realized by adding Bi atoms to this surface, and Ref. [50] showed that its surface states with large Rashba splitting around the Fermi energy are formed by covalent bonding between Bi atoms and Ag surface states. Therefore, the Ag surface states around 0.6 eV in Fig. 5h are stabilized by hybridization with the Bi sp_z band and exhibit the large Rashba splitting.

Thus the nodal lines near the Fermi level enhance the Rashba splitting at the surface in two ways. One is from the bulk polarization, coming from the π Zak phase, and the other is hybridization with the emergent surface states from the nodal lines. In Bi/Sr(111) the first scenario is dominant, whereas the second scenario dominates in Bi/Ag(111).

Summary– To summarize, the alkaline earth metals Ca, Sr and Yb have topological nodal lines near the Fermi level in the absence of the SOI, as shown by *ab initio* calculation. Ca becomes the NLS at high pressure. Apart from the known NLS's, the nodal lines do not lie on the mirror planes and purely come from topological origin characterized by π Berry phase. Consequently, the Zak phase is calculated to be either 0 or π , depending on the momentum. The π Zak phase leads to a polarization charge at the surface and after screening by carriers it induces surface dipoles and surface potential dip. The SOI gives rise to a small gap to the nodal line, while the surface states survive. Surface termination affects the surface states, while the Zak phase is unaffected. In the materials with nodal lines, both the large polarization and the emergent surface states enhance the Rashba splitting on the surface, as demonstrated in Bi/Sr(111) and in Bi/Ag(111).

Methods

Details of the first-principle calculation– We calculate the band structures within the density functional theory (DFT). We use *ab initio* code QMAS (Quantum Materials Simulator) and OpenMX. The electronic structure is calculated based on the local density approximation with/without the relativistic effect (LDA/LDA+SO). We also optimize the lattice parameter under pressure based on the generalized gradient approximation (GGA). The lattice parameter a for Ca/Sr/Yb/Ag is 5.5884/6.0849/5.4847/4.0853 Å. The plane-wave energy cutoff is set to 40/50 Ry for Ca, Sr, and Ag/Yb, and the

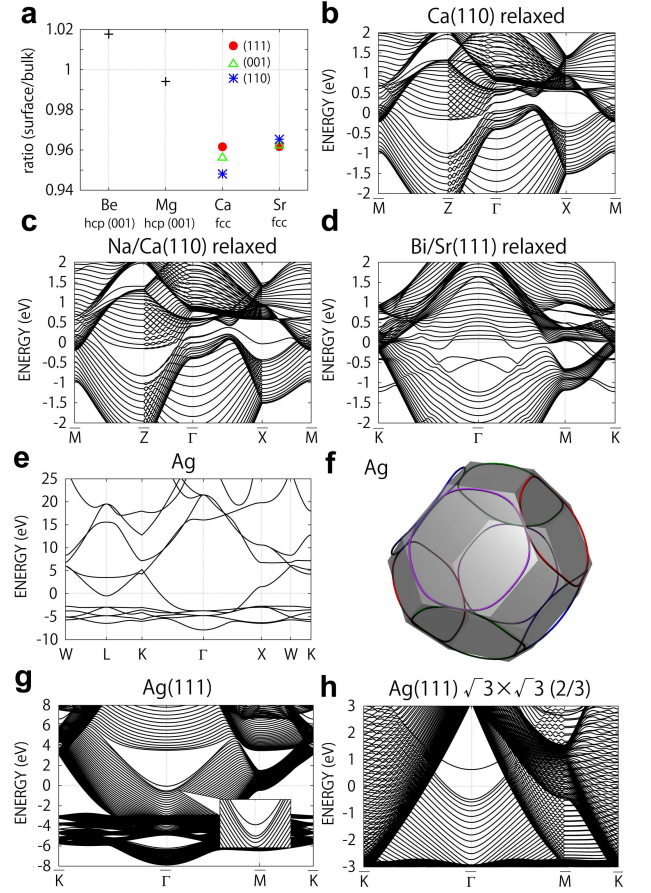


FIG. 5. Nodal line and Rashba effect. **a**, Ratio of the distance between the layers at the surface to that of bulk (20 layers). **b/c**, Electronic band structure of Ca for the (110) surface covered without/with Na in the LDA. **d**, Electronic band structure of Sr for the (111) surface covered with Bi in the LDA+SO. Structure is optimized by the GGA in **a,b,c,d**. **e**, Electronic band structure of Ag. **f**, Nodal lines around 5 eV and the Brillouin zone of Ag, where the nonequivalent nodal line is shown in the different color. **g/h**, Electronic band structure of Ag without/with long-range $\sqrt{3} \times \sqrt{3}$ structure on the (111) surface. The energy is measured from the Fermi level.

$12 \times 12 \times 12$ regular \mathbf{k} -mesh including the Γ point, with the Gaussian broadening of 0.025 eV, is employed. We construct the *spdf*-model for Ca, Sr, Yb, and Ag from the Kohn-Sham bands by the maximally localized Wannier function [51, 52]. Since the $4f$ orbital in Yb is fully occupied [53], we first make the *spdf*-model for Yb and disentangle out the $4f$ orbital from the model. We take 90/60 atoms in the calculation of the electronic band structure on the (110)/(111) and (001) surfaces (see Fig. 3b,d), 120/180 atoms in that on the (001)/(111) surface with long-range $\sqrt{2} \times \sqrt{2}/\sqrt{3} \times \sqrt{3}$ structure (see Fig. 4c,e,f) 30/20 atoms in that on the (110)/(111) surface with lattice relaxation (see Figs. 5b,c,d), and 45/135 atoms in that on the (111) surface without/with long-range $\sqrt{3} \times \sqrt{3}$ structure of Ag (see Fig. 5g,h). The electronic structure of Ag is calculated in the LDA (Fig. 5e,g,h). We take the vacuum region with thickness 20 Å for the slab calculation. Density of states at the Fermi level on the (110) surface is calculated by the surface Green's function [54, 55] where the system contains 720 atoms. (The electronic structure and lattice constant in Fig. 5 are calculated directly by the Kohn-Sham

Hamiltonian, and the other results in Figs. 2-5 are obtained via the Wannier function.)

Conditions for emergence of nodal lines– The reasons for emergence of nodal lines are classified into two, i.e. (A) mirror symmetry and (B) π Berry phase. For (A) systems with mirror symmetry, the states on the mirror plane are classified into two classes by the mirror eigenvalues. If the valence and conduction bands have different mirror eigenvalues, the two bands have no hybridization on the mirror plane, even if the two bands approach and cross. It results in a degeneracy along a loop on the mirror plane. This line-node degeneracy is protected by mirror symmetry, and once the mirror symmetry is broken, the degeneracy will be lifted in general. On the other hand, another mechanism based on (B) π Berry phase occurs for spinless systems with inversion and time-reversal symmetries. The Berry phase around the nodal line is π . In spinless systems with inversion and time-reversal symmetries, the Berry phase along any closed loop is quantized as an integer multiple of π , and therefore, the nodal line is topologically protected. In some materials the two mechanism coexist, whereas in others the loop originates from one of these mechanisms.

Calculation of the Zak phase along a reciprocal vector \mathbf{G} – We separate the Bloch wavevector \mathbf{k} into the components along $\mathbf{n} \equiv \mathbf{G}/|\mathbf{G}|$ and perpendicular to \mathbf{n} : $\mathbf{k} = k_{\perp}\mathbf{n} + \mathbf{k}_{\parallel}$, $\mathbf{k}_{\parallel} \perp \mathbf{n}$. The integral with respect to k_{\perp} is performed with fixed \mathbf{k}_{\parallel} . For each value of \mathbf{k}_{\parallel} , one can define the Zak phase by

$$\theta(\mathbf{k}_{\parallel}) = -i \sum_n^{\text{occ.}} \int_0^{2\pi/a_{\perp}} dk_{\perp} \langle u_n(\mathbf{k}) | \nabla_{k_{\perp}} | u_n(\mathbf{k}) \rangle, \quad (1)$$

where $u_n(\mathbf{k})$ is a bulk eigenstate in the n -th band, the sum is over the occupied states, and a_{\perp} is the size of the unit cell along the vector \mathbf{n} (see Supplemental Material). The gauge is taken to be $u_n(\mathbf{k}) = u_n(\mathbf{k} + \mathbf{G})e^{i\mathbf{G}\cdot\mathbf{r}}$. The Zak phase is defined modulo 2π . Under both inversion and time-reversal symmetries, the Zak phase is shown to take a quantized value 0 or $\pi \pmod{2\pi}$ [12, S1], as is also shown in the Supplemental Material. All the cases presented in this paper satisfy the symmetry conditions for the Zak phase to be quantized as 0 or π . In one-dimensional insulators, this formula (1) times $e/(2\pi)$ is equal to the polarization modulo e [S3]. In three-dimensional insulators, the polarization is calculated by multiplying the Zak phase with $e/2\pi$, and integrating over the momentum \mathbf{k}_{\parallel} perpendicular to \mathbf{G} . Thus this quantity is related with surface polarization charge for the surface perpendicular to \mathbf{n} [S3].

[1] Murakami, S. Phase transition between the quantum spin hall and insulator phases in 3D: emergence of a topological gapless phase. *New J. Phys.* **9**, 356 (2007).
[2] Wan, X., Turner, A. M., Vishwanath, A. & Savrasov, S. Y. Topological semimetal and Fermi-arc surface states in the electronic structure of pyrochlore iridates. *Phys. Rev. B* **83**, 205101 (2011).
[3] Wang, Z. *et al.* Dirac semimetal and topological phase transitions in $A_3\text{Bi}$ ($A = \text{Na, K, Rb}$). *Phys. Rev. B* **85**, 195320 (2012).
[4] Wang, Z., Weng, H., Wu, Q., Dai, X. & Fang, Z. Three-dimensional Dirac semimetal and quantum transport in Cd_3As_2 . *Phys. Rev. B* **88**, 125427 (2013).
[5] Mullen, K., Uchoa, B. & Glatzhofer, D. T. Line of dirac nodes in hyperhoneycomb lattices. *Phys. Rev. Lett.* **115**, 026403 (2015).
[6] Fang, C., Chen, Y., Kee, H.-Y. & Fu, L. Topological nodal line

semimetals with and without spin-orbital coupling. *Phys. Rev. B* **92**, 081201 (2015).
[7] Chen, Y. *et al.* Nanostructured carbon allotropes with Weyl-like loops and points. *Nano Lett.* **15**, 6974–6978 (2015).
[8] Weng, H. *et al.* Topological node-line semimetal in three-dimensional graphene networks. *Phys. Rev. B* **92**, 045108 (2015).
[9] Kim, Y., Wieder, B. J., Kane, C. L. & Rappe, A. M. Dirac line nodes in inversion-symmetric crystals. *Phys. Rev. Lett.* **115**, 036806 (2015).
[10] Yu, R., Weng, H., Fang, Z., Dai, X. & Hu, X. Topological node-line semimetal and Dirac semimetal state in antiperovskite Cu_3PdN . *Phys. Rev. Lett.* **115**, 036807 (2015).
[11] Xie, L. S. *et al.* A new form of Ca_3P_2 with a ring of Dirac nodes. *APL Mat.* **3** (2015).
[12] Chan, Y.-H., Chiu, C.-K., Chou, M. & Schnyder, A. P. Topological semi-metals with line nodes and drumhead surface states. Preprint at <http://arxiv.org/abs/1510.02759> (2015).
[13] Zeng, M. *et al.* Topological semimetals and topological insulators in rare earth monopnictides. Preprint at <http://arxiv.org/abs/1504.03492> (2015).
[14] Yamakage, A., Yamakawa, Y., Tanaka, Y. & Okamoto, Y.
[15] Zhao, J., Yu, R., Weng, H. & Fang, Z. Topological node-line semimetal in compressed black phosphorus. Preprint at <http://arxiv.org/abs/1511.05704> (2015).
[16] Liu, Z. K. *et al.* Discovery of a three-dimensional topological Dirac semimetal, Na_3Bi . *Science* **343**, 864–867 (2014).
[17] Xu, S.-Y. *et al.* Observation of Fermi arc surface states in a topological metal. *Science* **347**, 294–298 (2015).
[18] Neupane, M. *et al.* Observation of a three-dimensional topological Dirac semimetal phase in high-mobility Cd_3As_2 . *Nat. Commun.* **5**, 3786 (2014).
[19] Borisenko, S. *et al.* Experimental realization of a three-dimensional Dirac semimetal. *Phys. Rev. Lett.* **113**, 027603 (2014).
[20] Xu, G., Weng, H., Wang, Z., Dai, X. & Fang, Z. Chern semimetal and the quantized anomalous hall effect in HgCr_2Se_4 . *Phys. Rev. Lett.* **107**, 186806 (2011).
[21] Hirayama, M., Okugawa, R., Ishibashi, S., Murakami, S. & Miyake, T. Weyl node and spin texture in trigonal tellurium and selenium. *Phys. Rev. Lett.* **114**, 206401 (2015).
[22] Liu, J. & Vanderbilt, D. Weyl semimetals from non-centrosymmetric topological insulators. *Phys. Rev. B* **90**, 155316 (2014).
[23] Sun, Y., Wu, S.-C., Ali, M. N., Felser, C. & Yan, B. Prediction of Weyl semimetal in orthorhombic MoTe_2 . *Phys. Rev. B* **92**, 161107 (2015).
[24] Soluyanov, A. A. *et al.* Type-II Weyl semimetals. *Nature* **527**, 495–498 (2015).
[25] Huang, S.-M. *et al.* New type of Weyl semimetal with quadratic double Weyl fermions. *Proc. Natl. Acad. Sci. U.S.A.* (2016); published ahead of print January 19, 2016, doi:10.1073/pnas.1514581113
[26] Weng, H., Fang, C., Fang, Z., Bernevig, B. A. & Dai, X. Weyl semimetal phase in noncentrosymmetric transition-metal monophosphides. *Phys. Rev. X* **5**, 011029 (2015).
[27] Huang, S.-M. *et al.* A Weyl fermion semimetal with surface Fermi arcs in the transition metal monopnictide TaAs class. *Nat. Commun.* **6**, 7373 (2015).
[28] Lv, B. Q. *et al.* Experimental discovery of Weyl semimetal TaAs. *Phys. Rev. X* **5**, 031013 (2015).
[29] Xu, S.-Y. *et al.* Discovery of a Weyl fermion semimetal and topological Fermi arcs. *Science* **349**, 613–617 (2015).
[30] Lv, B. *et al.* Observation of Weyl nodes in TaAs. *Nat. Phys.* **11**, 724–727 (2015).

- [31] Xu, S.-Y. *et al.* Discovery of a Weyl fermion state with Fermi arcs in niobium arsenide. *Nat. Phys.* **11**, 748–754 (2015).
- [32] Yang, L. *et al.* Weyl semimetal phase in the non-centrosymmetric compound TaAs. *Nat. Phys.* **11**, 728–732 (2015).
- [33] Bian, G. *et al.* Drumhead surface states and topological nodal-line fermions in TiTaSe_2 . Preprint at <http://arxiv.org/abs/1508.07521> (2015).
- [34] Vasvari, B., Animalu, A. O. E., & Heine, V., Electronic Structure of Ca, Sr, and Ba under Pressure. *Phys. Rev.* **154**, 535 (1967).
- [35] Vasvari, B., Heine, V., The resistivity of calcium, strontium and barium under pressure. *Phil. Mag.* **15**, 731–738 (1967).
- [36] Ast, C. R., Henk, J., Ernst, A., Moreschini, L., Falub, M. C., Pacil , D., Bruno, P., Kern, K. & Grioni, M., Giant Spin Splitting through Surface Alloying. *Phys. Rev. Lett.* **98**, 186807 (2007).
- [37] Enderlein, C., Ramos, S. M., Bittencourt, M., Continentino, M. A., Brewer, W., & Baggio-Saitovich, E., Anomaly close to an electronic topological semimetal-insulator transition in elemental fcc-Yb under pressure. *J. Appl. Phys.* **114**, 143711 (2013).
- [38] McWhan, D. B., Rice, T. M. & Schmidt, P. H., *Phys. Rev.* **177**, 1063 (1969).
- [39] Magnitskaya, M. V., Matsko, N. L., Baturin, V. S., & Uspenskii, Y. A., Pressure-induced semimetallic behavior of calcium from *ab initio* calculations, *J. Phys. Conf. Ser.* **510**, 012028 (2014).
- [40] Jayaraman, A., Klement, Jr., W., & Kennedy, G. C., Phase Diagrams of Calcium and Strontium at High Pressures, *Phys. Rev.* **132**, 1620–1624 (1963).
- [41] Sakata, M., Nakamoto, Y., Shimizu, K., Matsuoka, T., & Ohishi, Y., Superconducting state of Ca-VII below a critical temperature of 29 K at a pressure of 216 GPa, *Phys. Rev. B* **83**, 220512(R) (2011).
- [42] Kariyado, T. & Hatsugai, Y. Symmetry-protected quantization and bulk-edge correspondence of massless Dirac fermions: Application to the fermionic Shastry-Sutherland model. *Phys. Rev. B* **88**, 245126 (2013).
- [43] Vanderbilt, D. & King-Smith, R. D. Electric polarization as a bulk quantity and its relation to surface charge. *Phys. Rev. B* **48**, 4442 (1993).
- [44] Ryu, S. & Hatsugai, Y. Topological origin of zero-energy edge states in particle-hole symmetric systems. *Phys. Rev. Lett.* **89**, 077002 (2002).
- [45] Mikitik, G. P. & Sharlai, Yu. V. Manifestation of Berry's Phase in Metal Physics. *Phys. Rev. Lett.* **82**, 2147 (1999).
- [46] Li, R., Cheng, X., Ma, H., Wang, S., Li, D., Zhang, Z., Li, Y., Chen, & X.-Q. Dirac node lines in pure alkali earth metals, Preprint at <http://arxiv.org/abs/1603.03974> (2016).
- [47] G. Bihlmayer, G., Koroteev, Yu. M., Echenique, P. M., Chulkov, E. V., Bl ugel, S. S. The Rashba-effect at metallic surfaces. *Surf. Sci.* **600**, 3888 (2006).
- [48] Gong, S.-J., Duan, C.-G., Zhu, Y., Zhu, Z.-Q., & Chu, J.-H., Controlling Rashba spin splitting in Au(111) surface states through electric field. *Phys. Rev. B* **87**, 035403 (2013).
- [49] Shanavas, K. V., & Satpathy, S., Electric Field Tuning of the Rashba Effect in the Polar Perovskite Structures. *Phys. Rev. Lett.* **112**, 086802 (2014).
- [50] Bian, G., Wang, X., Miller, T. & Chiang, T.-C., Origin of giant Rashba spin splitting in Bi/Ag surface alloys. *Phys. Rev. B* **88**, 085427 (2013).
- [51] Marzari, N. & Vanderbilt, D., Maximally localized generalized Wannier functions for composite energy bands. *Phys. Rev. B* **56**, 12847 (1997).
- [52] Souza, I., Marzari, N. & Vanderbilt, D., Maximally localized Wannier functions for entangled energy bands, *Phys. Rev. B* **65**, 035109 (2001).
- [53] Matsunami, M., Chainani, A., Taguchi, M., Eguchi, R., Ishida, Y., Takata, Y., Okamura, H., Nanba, T., Yabashi, M., Tamasaku, K., Nishino, Y., Ishikawa, T., Senba, Y., Ohashi, H., Tsujii, N., Ochiai, A. & Shin, S., Combining photoemission and optical spectroscopies for reliable valence determination in YbS and Yb metal, *Phys. Rev. B* **78**, 195118 (2008).
- [54] Turek, I., Drchal, V., Kudrnovsky, J., Sob, M. & Weinberger, P., *Electronic Structure of Disordered Alloys, Surfaces and Interfaces*, (Kluwer Academic, Boston, 1997).
- [55] Dai, X., Hughes, T. L., Qi, X.-L., Fang, Z. & Zhang, S.-C., Helical edge and surface states in HgTe quantum wells and bulk insulators. *Phys. Rev. B* **77**, 125319 (2008).

Acknowledgement

We thank Shoji Ishibashi for providing us with the *ab initio* code (QMAS) and pseudopotentials. This work was supported by Grant-in-Aid for Scientific Research (No. 26287062, 26600012), by the Computational Materials Science Initiative (CMSI), Japan, and also by MEXT Elements Strategy Initiative to Form Core Research Center (TIES).

Additional Information

The authors declare no competing financial interests.

Author contribution

All authors contributed to the main contents of this work. M.H. performed the *ab initio* calculation with contributions from T.M. R.O. constructed the arguments on the Zak phase and surface states. S.M. conceived and supervised the project. M.H., R.O. and S.M. drafted the manuscript. T.M. gave critical revisions of the manuscript.

Supplemental Materials

ZAK PHASE AND POLARIZATION

Decomposition of the wavevector components respecting the surface Brillouin zone

As a preparation for the calculation in the next subsection, we show the formula for decomposition of the wavevector \mathbf{k} into the surface normal k_\perp and the directions along the surface \mathbf{k}_\parallel . For the calculation of the Zak phase we use a formula

$$\theta(\mathbf{k}_\parallel) = -i \sum_n^{\text{occ.}} \int_0^{b_\perp} dk_\perp \langle u_n(\mathbf{k}) | \nabla_{k_\perp} | u_n(\mathbf{k}) \rangle, \quad (\text{S.1})$$

where b_\perp is the width of the Brillouin zone along the direction perpendicular to the surface. In fact, it is not obvious how to take the integration region, when the primitive vectors are not orthogonal to each other. In particular, as we show in the main text, we consider superstructure of the surface, and the primitive vectors may differ from the standard choice. Below we formulate the Brillouin zone of the crystal, which respects the surface periodicity.

Let $\mathbf{a}_{1\parallel}$ and $\mathbf{a}_{2\parallel}$ denote the primitive vectors along the surface. If surface superstructure is formed, these primitive vectors should be chosen accordingly. Then we add another vector \mathbf{a}' so that $\{\mathbf{a}_{1\parallel}, \mathbf{a}_{2\parallel}, \mathbf{a}'\}$ is a set of primitive vectors for the three-dimensional (3D) crystal, respecting the surface superstructure. (Thus it is not necessarily the primitive vectors of the 3D bulk crystal, but it is the minimal set of translation vectors which respects surface superstructure.)

Then we take the primitive reciprocal vectors $\{\mathbf{b}_1, \mathbf{b}_2, \mathbf{b}_\perp\}$ from $\{\mathbf{a}_{1\parallel}, \mathbf{a}_{2\parallel}, \mathbf{a}'\}$:

$$\mathbf{b}_1 = 2\pi \frac{\mathbf{a}_{2\parallel} \times \mathbf{a}'}{(\mathbf{a}_{1\parallel} \times \mathbf{a}_{2\parallel}) \cdot \mathbf{a}'}, \quad (\text{S.2})$$

$$\mathbf{b}_2 = 2\pi \frac{\mathbf{a}' \times \mathbf{a}_{1\parallel}}{(\mathbf{a}_{1\parallel} \times \mathbf{a}_{2\parallel}) \cdot \mathbf{a}'}, \quad (\text{S.3})$$

$$\mathbf{b}_\perp = 2\pi \frac{\mathbf{a}_{1\parallel} \times \mathbf{a}_{2\parallel}}{(\mathbf{a}_{1\parallel} \times \mathbf{a}_{2\parallel}) \cdot \mathbf{a}'} \quad (\text{S.4})$$

We note that \mathbf{b}_\perp is normal to the surface, whereas \mathbf{b}_1 and \mathbf{b}_2 are not necessarily along the surface (see Fig. S 1). We then project \mathbf{b}_1 and \mathbf{b}_2 onto the surface:

$$\mathbf{b}_{1\parallel} = \mathbf{b}_1 - \frac{\mathbf{b}_1 \cdot \mathbf{n}}{\mathbf{n} \cdot \mathbf{n}} \mathbf{n}, \quad (\text{S.5})$$

$$\mathbf{b}_{2\parallel} = \mathbf{b}_2 - \frac{\mathbf{b}_2 \cdot \mathbf{n}}{\mathbf{n} \cdot \mathbf{n}} \mathbf{n}, \quad (\text{S.6})$$

where \mathbf{n} is the unit vector normal to the surface. Then it follows that

$$\mathbf{a}_{i\parallel} \cdot \mathbf{b}'_{j\parallel} = 2\pi \delta_{ij} \quad (i, j = 1, 2) \quad (\text{S.7})$$

and therefore the set $\{\mathbf{b}_{1\parallel}, \mathbf{b}_{2\parallel}\}$ is a set of two-dimensional (2D) primitive reciprocal vectors for the surface, corresponding to

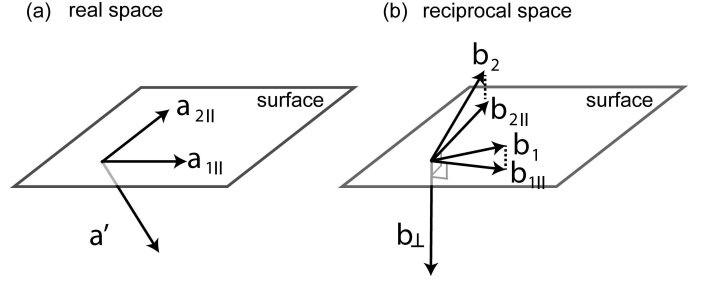


FIG. S 1. Translation vectors in \mathbf{a} real space and \mathbf{b} reciprocal space, used in our calculation

the 2D primitive vectors along the surface, $\{\mathbf{a}_{1\parallel}, \mathbf{a}_{2\parallel}\}$. Furthermore, the 3D Brillouin zone, which is a parallelogram spanned by $\{\mathbf{b}_1, \mathbf{b}_2, \mathbf{b}_\perp\}$, is equivalent to the parallelogram spanned by $\{\mathbf{b}_{1\parallel}, \mathbf{b}_{2\parallel}, \mathbf{b}_\perp\}$, with \mathbf{b}_\perp perpendicular to the surface. Therefore, in Eq. (S.1), we take the k_\perp to be from zero to b_\perp , while \mathbf{k}_\parallel takes a 2D wavevector within the 2D Brillouin zone spanned by $\{\mathbf{b}_{1\parallel}, \mathbf{b}_{2\parallel}\}$. We note that b_\perp is equal to $2\pi/a'_\perp$, where a'_\perp is a surface-normal component of \mathbf{a}' .

Symmetry properties of the Zak phase in three dimensions

Here we note on symmetry properties of the Zak phase. We first review the results shown in previous works [S2, S3], and then we discuss results on the nodal-line semimetals. We first rewrite the Schrödinger equation $\mathcal{H}\psi_k = E_k\psi_k$ in terms of the Bloch wavefunction, where \mathcal{H} is the Hamiltonian, \mathbf{k} is the Bloch wavefunction, ψ_k is the wavefunction, and E_k is the energy. Throughout the paper, we adopt the gauge

$$\psi_{\mathbf{k}+\mathbf{G}} = \psi_{\mathbf{k}}, \quad (\text{S.8})$$

where \mathbf{G} is any reciprocal lattice vector, as in [S2, S3]; this gauge choice is necessary for relating the Zak phase $\theta(\mathbf{k}_\parallel)$ with polarization. Then we get

$$\hat{H}_k u_k = E_k u_k, \quad (\text{S.9})$$

where $\psi_k = u_k e^{i\mathbf{k} \cdot \mathbf{r}}$ and $\hat{H}_k \equiv e^{-i\mathbf{k} \cdot \mathbf{r}} \mathcal{H} e^{i\mathbf{k} \cdot \mathbf{r}}$. The gauge choice (S.8) is rewritten as $u_k = u_{\mathbf{k}+\mathbf{G}} e^{i\mathbf{k} \cdot \mathbf{r}}$.

Zak phase around the nodal line and the Zak phase

When the inversion and time-reversal symmetries are present in spinless systems, the Zak phase $\theta(C)$ around any closed loop C is quantized as

$$\theta(C) \equiv -i \sum_n^{\text{occ.}} \oint_C d\mathbf{k} \cdot \langle u_n(\mathbf{k}) | \nabla_{\mathbf{k}} | u_n(\mathbf{k}) \rangle = n\pi \quad (n : \text{integer}). \quad (\text{S.10})$$

In particular, the Berry phase around the nodal line (contour c in Fig. S 2) is π , and thanks to the above quantization, the

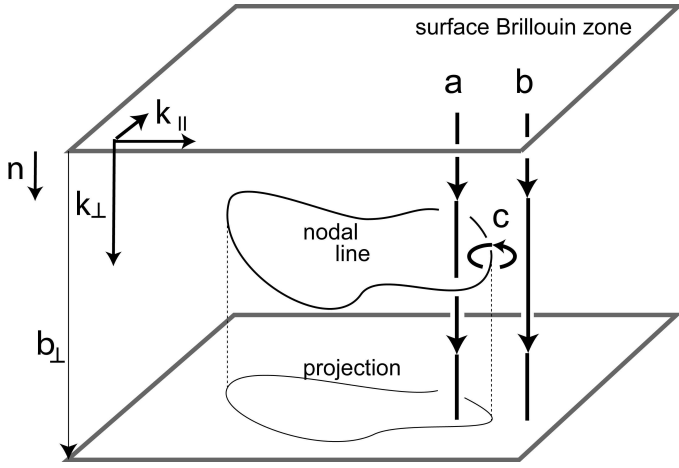


FIG. S 2. Relation between the Zak phases (Berry phase) along the surface normal (paths a,b) and the Berry phase around the nodal line.

nodal line is topologically protected. Thus the Zak phases (Berry phase) along the surface normal k_{\perp} changes by π , when k_{\parallel} is changed across the projection of the nodal line onto the surface. In Fig. S 2 the Zak phases for the paths a and b are different by π , which is the Berry phase around the loop c around the nodal line.

Symmetry properties of the Zak phase

In the following we show consequences on $\theta(\mathbf{k}_{\parallel})$ from the symmetries of the system.

(i) Inversion symmetry

When the system has inversion symmetry, we have

$$[\mathcal{P}, \mathcal{H}] = 0 \Rightarrow \mathcal{P} \hat{H}_k \mathcal{P}^{-1} = H_{-k}, \quad (\text{S.11})$$

where \mathcal{P} is the inversion operator. Then we can derive the relationship of the Zak phase:

$$\theta(\mathbf{k}_{\parallel}) \equiv -\theta(-\mathbf{k}_{\parallel}) \pmod{2\pi}. \quad (\text{S.12})$$

As compared with the present result, the results in Ref. [S1] contains an additional term. This is due to different choices of gauge; in Ref. [S1] the gauge $u_k = u_{k+G}$ is adopted, whereas we adopt the gauge (S.8), which is directly related with the polarization.

(ii) Time-reversal symmetry

When the system has time-reversal symmetry, we have

$$[\mathcal{K}, \mathcal{H}] = 0 \Rightarrow \mathcal{K} \hat{H}_k \mathcal{K} = H_{-k}, \quad (\text{S.13})$$

where \mathcal{K} is the complex conjugation. Here we focus on spinless systems, where the time-reversal operation is represented as \mathcal{K} . Then the Zak phase satisfies

$$\theta(-\mathbf{k}_{\parallel}) \equiv \theta(\mathbf{k}_{\parallel}) \pmod{2\pi}. \quad (\text{S.14})$$

It is the same as that in Ref. [S1], although the gauges are different from ours.

(iii) Inversion and time-reversal symmetries

Therefore, from these results (i) and (ii), when the system has both time-reversal and inversion symmetries, Eqs. (S.12) and (S.14) yield

$$\theta(\mathbf{k}_{\parallel}) \equiv 0 \text{ or } \pi \pmod{2\pi}. \quad (\text{S.15})$$

We consider an implication of Eq. (S.15) for insulators and for nodal-line semimetals in the following.

Zak phase, polarization, and surface polarization charge

In Ref. [S3], the relationship between the Zak phase and the surface polarization charge density σ is found. The surface polarization charge density, i.e. the surface normal component of the polarization vector, is given by

$$\sigma = \sigma_{\text{ion}} + \sigma_e \quad (\text{S.16})$$

where σ_{ion} is an ionic contribution from surface atoms, and σ_e represents an electronic contribution

$$\sigma_e = \int \frac{d^2 k_{\parallel}}{(2\pi)^2} \sigma_e(\mathbf{k}_{\parallel}), \quad \sigma_e(\mathbf{k}_{\parallel}) \equiv \frac{-e}{2\pi} \theta(\mathbf{k}_{\parallel}) \pmod{e}. \quad (\text{S.17})$$

If we regard the system at fixed \mathbf{k}_{\parallel} to be a one-dimensional system, $\sigma_e(\mathbf{k}_{\parallel})$ is an electronic surface charge density for the one-dimensional subsystem at \mathbf{k}_{\parallel} [S3].

We first consider insulators, and we assume that there is no surface state that crosses the Fermi energy. Then $\sigma_e(\mathbf{k}_{\parallel})$ does not have a jump as a function of \mathbf{k}_{\parallel} . Therefore, from Eq. (S.15), $\sigma_e(\mathbf{k}_{\parallel})$ is independent of \mathbf{k}_{\parallel} :

$$\sigma_e(\mathbf{k}_{\parallel}) = N \frac{e}{2}, \quad (\text{S.18})$$

where N is an integer constant. Therefore, the surface charge density is $\sigma_e = \frac{Ne}{2A_{\text{surface}}}$ where A_{surface} is an area of the surface unit cell [S3]. While N can be any integer, it is physically expected to vanish in almost all the insulators, because nonzero N corresponds to a giant polarization, liable to chemical or electronic instability. Thus $N = 0$ is expected to be chosen as stable electronic states, and so far no insulator is known to have nonzero integer N , giving rise to a huge surface polarization.

Meanwhile, in materials with nodal lines which are the focus of the present work, the Zak phase jumps by π at the nodal lines, and therefore there is always a region with $\theta(\mathbf{k}_{\parallel}) \equiv 0 \pmod{2\pi}$ and that with $\theta(\mathbf{k}_{\parallel}) \equiv \pi \pmod{2\pi}$. The latter region leads to an appreciable polarization. In nodal-line semimetals, the bulk electronic carriers and ions will eventually screen the polarization, but there occurs a large deformation of the lattice structure and surface dipoles. It is expected to lead to large Rashba splitting if adatoms with large spin-orbit coupling are present, as shown in the main text.

SURFACE TERMINATION AND CHOICE OF THE UNIT CELL

The surface polarization charge density σ_e is related with the polarization vector \mathbf{P} as $\sigma = P_\perp \equiv \mathbf{P} \cdot \mathbf{n}$, where \mathbf{n} is a unit vector normal to the surface. Even when the direction of the surface plane is fixed such as (111) or (001), there are some possibilities for surface terminations. Moreover, for a given surface termination there are various possible choices for the unit cell.

The dependence on the choice of the unit cell is discussed in Ref. [S3]. To summarize the results in Ref. [S3], for a fixed surface termination, the polarization $\sigma (= P_\perp)$ is independent of the choice of the unit cell of the bulk. To be more precise, if one changes the unit cell for a fixed surface termination, σ is independent of the choice of the unit cell, whereas each of the two contributions σ_e and σ_{ion} in Eq. (S.16) may depend on the unit cell choice.

On the other hand, if the surface termination is changed, σ generally changes. In the following we consider several cases of surface terminations for the (001) and (111) surfaces. For the calculations we will always choose the unit cell in such a way that there are no extra “surface atoms”, which are excess atoms that are not covered by the unit cell with primitive translations, as explained in Ref. [S3]. With such a choice of unit cell, we always have $\sigma_{\text{ion}} = 0$ and we have only to consider the dependence of the electronic part σ_e .

Thus in the following discussion of various surface terminations, the unit cell is chosen accordingly. According to ref. [S1], because the change of the choice of the unit cell corresponds to the unitary transformation of the Hamiltonian, the change of the unit cell choice affects the Zak phase in the following way. Suppose the unit structure consists of N atoms at $\{\mathbf{r}_1, \dots, \mathbf{r}_N\}$. If the unit cell convention is changed to $\{\mathbf{r}_1 + \boldsymbol{\epsilon}_1, \dots, \mathbf{r}_N + \boldsymbol{\epsilon}_N\}$ where $\boldsymbol{\epsilon}_a$ ($a = 1, \dots, N$) are translation vectors of the crystal, the change of the Zak phase $\Delta\theta'(\mathbf{k}_\parallel)$ is expressed as [S1]

$$\Delta\theta'(\mathbf{k}_\parallel) = -2\pi \sum_{a=1}^N \boldsymbol{\epsilon}_a^\perp \rho_a(\mathbf{k}_\parallel), \quad (\text{S.19})$$

where $\boldsymbol{\epsilon}_a^\perp$ is a surface-normal component of $\boldsymbol{\epsilon}_a$, and

$$\rho_a(\mathbf{k}_\parallel) \equiv \sum_m^{\text{occ.}} \int_0^{b_\perp} \frac{dk_\perp}{2\pi} \langle u_{nk} | \mathcal{P}_a | u_{nk} \rangle. \quad (\text{S.20})$$

Here \mathcal{P}_a ($a = 1, \dots, N$) is a projection operator projecting onto the atom a .

In the present framework, $\boldsymbol{\epsilon}_a$ is a translation vector, which is a linear combination of $\{\mathbf{a}_{1\parallel}, \mathbf{a}_{2\parallel}, \mathbf{a}'\}$ with integer coefficients. Among these primitive vectors, only \mathbf{a}' has a nonzero surface-normal component. Hence, $\boldsymbol{\epsilon}_a^\perp$ is an integer multiple of a'_\perp .

(001) surface

On the (001) surface, when half of the surface atoms are depleted, the $\sqrt{2} \times \sqrt{2}$ structure is formed. Therefore, from the outset we consider the unit cell for the 2D surface with enlarged unit cell for the $\sqrt{2} \times \sqrt{2}$ structure. Let a denote the lattice constant for the cubic unit cell of the fcc lattice. Then the primitive vectors for the 2D surface can be taken as

$$\mathbf{a}_{1\parallel} = a(1, 0, 0), \quad \mathbf{a}_{2\parallel} = a(0, 1, 0) \quad (\text{S.21})$$

Then another primitive vector is given by $\mathbf{a}' = a(\frac{1}{2}, 0, \frac{1}{2})$. The unit cell spanned by $\{\mathbf{a}_{1\parallel}, \mathbf{a}_{2\parallel}, \mathbf{a}'\}$ contains two atoms. Then we have

$$\mathbf{b}_1 = \frac{2\pi}{a}(1, 0, -1), \quad \mathbf{b}_2 = \frac{2\pi}{a}(0, 1, 0), \quad \mathbf{b}_\perp = \frac{4\pi}{a}(0, 0, 1). \quad (\text{S.22})$$

Hence we have,

$$\mathbf{b}_{1\parallel} = \frac{2\pi}{a}(1, 0, 0), \quad \mathbf{b}_{2\parallel} = \frac{2\pi}{a}(0, 1, 0). \quad (\text{S.23})$$

For the perfect (001) surface on the xy plane (Fig. S 3a), the unit structure consists of the two atoms at $(0, 0, 0)$ and $\mathbf{c} = a(-\frac{1}{2}, \frac{1}{2}, 0)$. Let us call the two sublattices I, and II which belong to the points 0, and \mathbf{c} , respectively. When the atoms at $a(m + \frac{1}{2}, n + \frac{1}{2})$ (m, n : integer) are depleted (Fig. S 3b), the surface forms a $\sqrt{2} \times \sqrt{2}$ structure, and the unit structure consists of the two atoms at $(0, 0, 0)$ and $\mathbf{c} + \mathbf{a}' = a(0, \frac{1}{2}, \frac{1}{2})$. Both of the two choices of the unit structure are inversion symmetric, and therefore in both cases the Zak phase is quantized as 0 or $\pi \pmod{2\pi}$. Thus in the new choice of unit structure, the atom in the sublattice II is shifted by \mathbf{a}' , and

$$\Delta\theta'(\mathbf{k}_\parallel) = -2\pi \mathbf{a}'_\perp \rho_{\text{II}}(\mathbf{k}_\parallel), \quad (\text{S.24})$$

$$\rho_{\text{II}}(\mathbf{k}_\parallel) \equiv \sum_m^{\text{occ.}} \int_0^{b_\perp} \frac{dk_\perp}{2\pi} \langle u_{nk} | \mathcal{P}_{\text{II}} | u_{nk} \rangle. \quad (\text{S.25})$$

By noting that the two sublattices are equivalent, we get $\langle u_{nk} | \mathcal{P}_{\text{I}} | u_{nk} \rangle = \frac{1}{2} \langle u_{nk} | u_{nk} \rangle = \frac{1}{2}$ ($a = \text{I, II}$), and $\rho_{\text{II}}(\mathbf{k}_\parallel) = \sum_m^{\text{occ.}} \frac{1}{2} \frac{b_\perp}{2\pi} = \frac{N_{\text{occ.}}}{2} \frac{b_\perp}{2\pi}$, where $N_{\text{occ.}}$ is the number of occupied bands. Thus

$$\Delta\theta(\mathbf{k}_\parallel) = -\frac{N_{\text{occ.}}}{2} a'_\perp b_\perp = -\frac{N_{\text{occ.}}}{2} 2\pi \quad (\text{S.26})$$

Lastly we note that the unit cell is doubled from the original fcc unit cell, and therefore $N_{\text{occ.}}$ is even. Thus the Zak phase is unchanged: $\Delta\theta(\mathbf{k}_\parallel) \equiv 0 \pmod{2\pi}$, in accordance with the *ab initio* calculation in the main text.

(111) surface

On the (111) surface, when 1/3 or 2/3 of the surface atoms are depleted, the $\sqrt{3} \times \sqrt{3}$ structure is formed. Therefore, from the outset we consider the unit cell for the 2D surface with enlarged unit cell for the $\sqrt{3} \times \sqrt{3}$ structure. While the standard

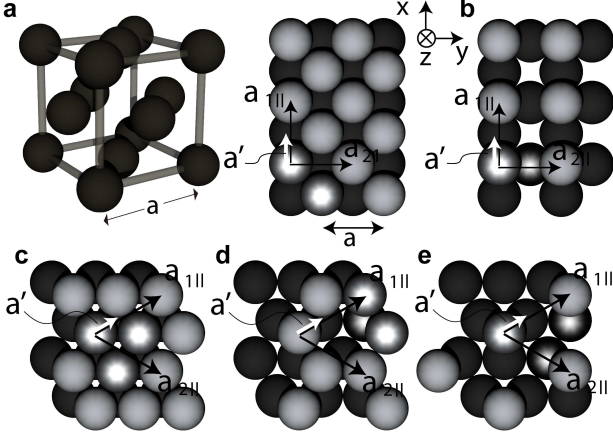


FIG. S 3. **a**, Crystal structure of fcc Ca, Sr, and Yb, and that of the (001) surface (black circle) with surface atoms (gray circle). **b** shows the same surface orientation but with (1/2) atoms per unit cell on the surface. **c**, Crystal structure of the (111) surface (black circle) with surface atoms (gray circle). **d** and **e** show the same surface orientation but with (1/3) and (2/3) atoms per unit cell on the surface, respectively. In **a-e**, the primitive vectors $\tilde{a}_{1||}$, $\tilde{a}_{2||}$ along the surface are shown as black arrows, while, the other primitive vector \tilde{a}' is shown as a white arrow. In **a-e**, the choice of the unit structure is marked by the circles with gradation, i.e. in **a,b** the unit structure consists of two atoms while in **c,d,e** it consists of three atoms.

choice of the primitive vectors are $\tilde{a}_{1||} = \frac{a}{\sqrt{2}}(0, 1, 0)$, $\tilde{a}_{2||} = \frac{a}{2\sqrt{2}}(-\sqrt{3}, 1, 0)$, the primitive vectors for the $\sqrt{3} \times \sqrt{3}$ structure can be taken as

$$\mathbf{a}_{1||} = \frac{a}{2\sqrt{2}}(\sqrt{3}, 3, 0), \quad \mathbf{a}_{2||} = \frac{a}{2\sqrt{2}}(-\sqrt{3}, 3, 0) \quad (\text{S.27})$$

Then another primitive vector is given by $\mathbf{a}' = \frac{a}{6\sqrt{2}}(\sqrt{3}, 3, 2\sqrt{6})$. The unit cell spanned by $\{\mathbf{a}_{1||}, \mathbf{a}_{2||}, \mathbf{a}'\}$ contains three atoms. Then we have

$$\mathbf{b}_1 = \frac{2\pi}{3a}(\sqrt{6}, \sqrt{2}, -\sqrt{3}), \quad \mathbf{b}_2 = \frac{2\sqrt{2}\pi}{3a}(-\sqrt{3}, 1, 0), \quad (\text{S.28})$$

$$\mathbf{b}_\perp = \frac{2\sqrt{3}\pi}{a}(0, 0, 1) \quad (\text{S.29})$$

Hence we have,

$$\mathbf{b}_{1||} = \frac{2\sqrt{2}\pi}{3a}(\sqrt{3}, 1, 0), \quad \mathbf{b}_{2||} = \frac{2\sqrt{2}\pi}{3a}(-\sqrt{3}, 1, 0). \quad (\text{S.30})$$

For the perfect (111) surface on the xy plane (Fig. S 3c), the unit structure consists of the three atoms at $\{0, \tilde{a}_{1||}, \tilde{a}_{2||}\}$. Let us call the three sublattices I, II and III which belongs to the points $0, \tilde{a}_{1||}$, and $\tilde{a}_{2||}$, respectively. When the 1/3 atoms are depleted (Fig. S 3d), the unit structure consists of the three atoms at $\{0, \tilde{a}_{1||} + \mathbf{a}', \tilde{a}_{2||}\}$. Thus in the new choice of unit structure, the atom in the sublattice II is shifted by \mathbf{a}' , and

$$\Delta\theta(\mathbf{k}_{||}) = -2\pi\mathbf{a}'_\perp \rho_{\text{II}}(\mathbf{k}_{||}), \quad (\text{S.31})$$

$$\rho_{\text{II}}(\mathbf{k}_{||}) \equiv \sum_m^{\text{occ.}} \int_0^{b_\perp} \frac{dk_\perp}{2\pi} \langle u_{nk} | \mathcal{P}_{\text{II}} | u_{nk} \rangle. \quad (\text{S.32})$$

By noting that the three sublattices are equivalent, we get $\langle u_{nk} | \mathcal{P}_{\text{a}} | u_{nk} \rangle = \frac{1}{3} \langle u_{nk} | u_{nk} \rangle = \frac{1}{3}$ ($a = \text{I, II, III}$), and $\rho_{\text{II}}(\mathbf{k}_{||}) = \sum_m^{\text{occ.}} \frac{1}{3} \frac{b_\perp}{2\pi} = \frac{N_{\text{occ.}}}{3} \frac{b_\perp}{2\pi}$, where $N_{\text{occ.}}$ is the number of occupied bands. Thus

$$\Delta\theta(\mathbf{k}_{||}) = -\frac{N_{\text{occ.}}}{3} \mathbf{a}'_\perp b_\perp = -\frac{N_{\text{occ.}}}{3} 2\pi \quad (\text{S.33})$$

Lastly we note that the unit cell is tripled from the original fcc unit cell, and therefore $N_{\text{occ.}}$ is a integer multiple of three. Thus the Zak phase is unchanged: $\Delta\theta(\mathbf{k}_{||}) \equiv 0 \pmod{2\pi}$,

When the 2/3 atoms are depleted (Fig. S 3e), the unit structure consists of the three atoms at $\{0, \tilde{a}_{1||} + \mathbf{a}', \tilde{a}_{2||} + \mathbf{a}'\}$.

With the similar calculation we get

$$\Delta\theta'(\mathbf{k}_{||}) = -2\pi(\mathbf{a}'_\perp \rho_{\text{II}}(\mathbf{k}_{||}) + \mathbf{a}'_\perp \rho_{\text{III}}(\mathbf{k}_{||})), \quad (\text{S.34})$$

$$\rho_{\text{II}}(\mathbf{k}_{||}) = \rho_{\text{III}}(\mathbf{k}_{||}) = \frac{N_{\text{occ.}}}{3} \frac{b_\perp}{2\pi}. \quad (\text{S.35})$$

Therefore

$$\Delta\theta(\mathbf{k}_{||}) = -\frac{2N_{\text{occ.}}}{3} 2\pi \equiv 0 \pmod{2\pi} \quad (\text{S.36})$$

and the Zak phase is unchanged in accordance with the *ab initio* calculation in the main text. We also note that in these three choices of the unit structure, the Zak phase is quantized as 0 or $\pi \pmod{2\pi}$.

\mathbb{Z}_2 TOPOLOGY OF THE NODAL LINES IN ALKALINE-EARTH METALS

In Ref. [S4] a \mathbb{Z}_2 topological number is defined for each nodal line in spinless systems with both inversion and time-reversal symmetries. If it is nontrivial, the nodal line cannot vanish by itself after shrinking to a point. This \mathbb{Z}_2 topological number can be defined for each nodal line in Ca, when the spin-orbit coupling is neglected, and it turns out to be trivial. It is because by adding an artificial potential for the 4s orbital by hand, the nodal lines around the L points disappear (see Fig. S 4a-c).

Similar analysis on the nodal lines around 5 eV in Ag (Fig. S 4d) shows that it is also \mathbb{Z}_2 -trivial in the sense of Ref. [S4]. Figures S4e,f show disappearance of the nodal line by decreasing the on-site potential of the 5s orbital.

SCREENING IN NODAL-LINE SEMIMETALS

When the nodal-line semimetal is regarded as a set of independent one-dimensional systems for individual values of $\mathbf{k}_{||}$, we have shown in the main text that within a \mathbf{k} -space region of π Zak phase there is an appreciable polarization of $\pm e/2$. Nevertheless, since the entire system is a semimetal with carriers, the polarization charges at the surface will be eventually screened. In this section we consider screening of the surface polarization charges in nodal-line semimetals by carriers.

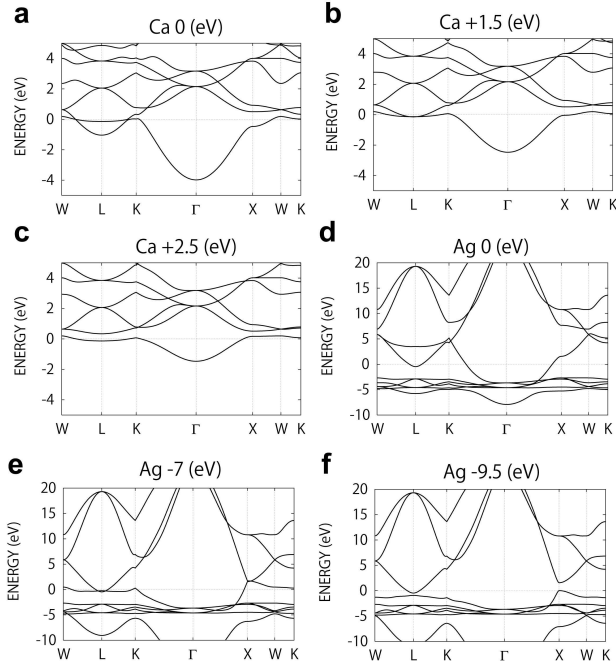


FIG. S 4. **a**, Electronic band structure of Ca in the LDA. **b/c**, Electronic band structure of Ca, where we add 1.5/2.5 eV to the on-site potential of the s orbital. **d**, Electronic band structure of Ag in the LDA. **d/f**, Electronic band structure of Ag, where we subtract 7/9.5 eV to the on-site potential of the s orbital.

For simplicity, we consider the nodal-line semimetal with its nodal line being a circle in k_x - k_y plane with radius k_0 , and we assume the dispersion perpendicular to the nodal line to be linear with velocity v_0 . Then the dispersion is represented as

$E = \pm \hbar v_0 \sqrt{(\sqrt{k_x^2 + k_y^2} - k_0)^2 + k_z^2}$. Then the density of states is $\nu(E) = C|E|$ with $C = \frac{k_0}{2\pi v_0^2 \hbar^2}$ per unit volume. In calcium there are four nodal lines, and therefore the constant C is multiplied by the number of nodal lines $g(=4)$; $C = \frac{gk_0}{2\pi v_0^2 \hbar^2}$

The Poisson equation is

$$\frac{d^2 V}{dz^2} = \frac{e}{\epsilon_0 \epsilon} \rho \quad (\text{S.37})$$

where $\rho(z)$ is the charge density, and V is the potential energy for electrons, based on Ref. [S5]. We set the z -axis normal to the surface into the semimetal, with $z = 0$ representing the surface.

We suppose that the polarization charge appears at the surface by the presence of nodal lines, with the polarization charge density σ_s . For example in Ca surface, as we have shown in the main text, the nodal line depletes electrons at the surface within the area in \mathbf{k} space surrounded by the nodal lines (shown as the shaded region in Fig. 3h), and polarization charge is positive: $\sigma_s > 0$. Then electron carriers are induced near the surface due to this positive surface charge, and $V(z) < 0$ is expected near the surface. The following equation

relates the charge density ρ with the potential V ,

$$\rho(z) = -en(z), \quad n(z) = \int_0^\infty f_F(E, z) \nu(E) dE, \quad (\text{S.38})$$

where $f_F(E, z) = \frac{1}{e^{\beta(E - E_F + V(z))} + 1}$ is the Fermi distribution function in the presence of potential $V(z)$. For simplicity we consider zero temperature and $E_F = 0$ (i.e. at the nodal line), and we have

$$n(z) = \frac{1}{2} C V(z)^2 \quad (\text{S.39})$$

From Eqs. (S.37) (S.38) and (S.39), we get

$$\frac{d^2 V}{dz^2} = -\frac{e^2 C}{2\epsilon_0 \epsilon} V^2 \quad (\text{S.40})$$

with boundary conditions $V(z = \infty) = 0$, $V'(z = 0) = \frac{e}{\epsilon_0 \epsilon} \sigma_s$. The solution is

$$V(z) = -\frac{e\lambda\sigma_s}{2\epsilon_0 \epsilon} \frac{1}{(1 + z/\lambda)^2}, \quad (\text{S.41})$$

where $\lambda = \left(\frac{24\epsilon_0^2 e^2}{e^3 C \sigma_s}\right)^{1/3}$ represents a screening length. The charge distribution is

$$n(z) = \frac{1}{2} C V^2 = \frac{C}{8} \left(\frac{e\lambda\sigma_s}{\epsilon_0 \epsilon}\right)^2 \frac{1}{(1 + z/\lambda)^4} \quad (\text{S.42})$$

The spatial dependence of the potential $V(z)$ and electron density $n(z)$ are plotted in Fig. S 5. The total induced charge density is calculated as $\sigma_{\text{ind}} = -e \int_0^\infty n dz = -\sigma_s$. Therefore, the induced electronic distribution totally screens the positive polarization charge at the surface. Meanwhile, there remains a finite dipole moment, whose density is calculated as

$$-e \int_0^\infty n z dz = -\frac{\sigma_s \lambda}{2} \quad (\text{S.43})$$

By putting $\epsilon = 5$, $\sigma_s \sim 0.243e/A_{\text{surface}}$, $A_{\text{surface}} = 1.5 \times 10^{-19} \text{m}^2$, $v_0 \sim 3 \times 10^5 \text{m/s}$, $k_0 \sim 0.24 \text{nm}^{-1}$ as a rough estimate of calcium at 7.5 GPa, the screening length is estimated as $\lambda \sim 0.24 \text{nm}$, i.e. of the order of a lattice constant, and the depth of the potential $V_0 \equiv V(z = 0) = -\frac{e\lambda\sigma_s}{2\epsilon_0 \epsilon}$ is about -0.77eV . The dipole density (per surface unit cell) is $0.243e \cdot 0.24 \text{nm}/2 = 4.7 \times 10^{-21} \text{C} \cdot \text{nm}$, and the electric field at the surface is $-2V_0/(e\lambda) = 6.4 \text{V/nm}$.

So far we have studied the screening by bulk carriers, and we found that the dipoles are formed at the surface, and the electronic potential is lowered near the surface as shown in Fig. S 5, This will affect surface states, if any, as we see below. Figure S 6 shows our result of the band structure of the Ca slab at 7.5GPa with (111) surfaces, by full self-consistent slab calculations with the lattice being fixed. As we compare Fig. 3g (without electronic relaxation) and Fig. S 6a (with electronic relaxation), we see that surface states come down to the Fermi energy, within the grey region in Fig. S 6b, and some of the surface states come even below the Fermi energy

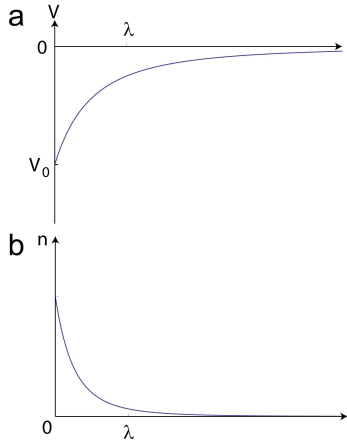


FIG. S 5. Spatial dependence of the potential $V(z)$ (a) and electron density (b).

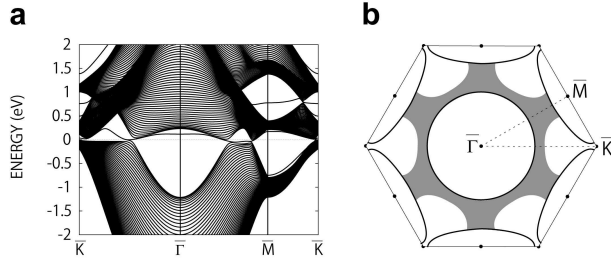


FIG. S 6. **a**, Electronic band structure of Ca at 7.5 GPa for the (111) surface in the LDA, with the lattice is fixed. **b**, (grey) Region in the surface Brillouin zone, where the surface states come below the Fermi energy by relaxation. The solid curves are projections of nodal lines.

to become occupied (shown as the shaded region in Fig. S 6b). This lowering of surface states is attributed to the negative potential $V(z)$ near the surface. Because the potential $V(z)$ is localized close to the surface, the surface states with shorter penetration depth is more affected by the potential $V(z)$. The maximum of the energy shift of the surface state is expected to be V_0 and it has been estimated to be around -0.77eV . This estimate is in good agreement with the energy shift of the surface states between Fig. 3g (without electronic relaxation) and Fig. S 6a (with electronic relaxation). Thus, to summarize, the surface polarization charge due to the nodal lines are partially screened by the bulk carriers, leaving behind dipoles at the surface. It induces an electronic potential which affects surface states, if there are any surface states within the energy scale of the potential $V(z)$ at the surface.

-
- [S1] Kariyado, T. & Hatsugai, Y. Symmetry-protected quantization and bulk-edge correspondence of massless Dirac fermions: Application to the fermionic Shastry-Sutherland model. *Phys. Rev. B* **88**, 245126 (2013).
 - [S2] Zak, J. Zak's phase for Energy Bands in Solids. *Phys. Rev. Lett.* **62**, 2747359 (2982).
 - [S3] Vanderbilt, D. & King-Smith, R. D. Electric polarization as a bulk quantity and its relation to surface charge. *Phys. Rev. B* **48**, 4442 (1993).
 - [S4] Fang, C., Chen, Y., Kee, H.-Y. & Fu, L. Topological nodal line semimetals with and without spin-orbital coupling. *Phys. Rev. B* **92**, 081201 (2015).
 - [S5] Zöllner, J. -P., Übensee, H., Paasch, G., Fiedler, T. & Gobsch, G. A Novel Self-Consistent Theory of the Electronic Structure of Inversion Layers in InSb MIS Structures, *Phys. Stat. Sol. (b)* **134**, 837 (1986).